ACCOUNTS of chemical research

Article

Cite This: Acc. Chem. Res. 2018, 51, 1433−1442

pubs.acs.org/accounts

State-Resolved Metal Nanoparticle Dynamics Viewed through the Combined Lenses of Ultrafast and Magneto-optical Spectroscopies

Tian Zhao, Patrick J. Herbert, Hongjun Zheng, and Kenneth L. Knappenberger, Jr.*

Department of Chemistry, The Pennsylvania State University, University Park, Pennsylvania 16802, United States

CONSPECTUS: Electronic carrier dynamics play pivotal roles in the functional properties of nanomaterials. For colloidal metals, the mechanisms and influences of these dynamics are structure dependent. The coherent carrier dynamics of collective plasmon modes for nanoparticles (approximately 2 nm and larger) determine optical amplification factors that are important to applied spectroscopy techniques. In the nanocluster domain (sub-2 nm), carrier coupling to vibrational modes affects photoluminescence yields. The performance of photocatalytic materials featuring both nanoparticles and nanoclusters also depends on the relaxation dynamics of nonequilibrium charge carriers. The challenges for developing comprehensive descriptions of carrier dynamics spanning both domains are multifold. Plasmon coherences are short-lived, persisting for only tens of femtoseconds. Nanoclusters exhibit discrete carrier dynamics that can persist for microseconds in some cases. On this time scale, many state-dependent processes, including vibrational relaxation, charge transfer, and spin conversion, affect carrier dynamics in ways that are nonscalable but, rather, structure specific. Hence, state-resolved spectroscopy methods are needed for understanding carrier dynamics in the nanocluster domain.

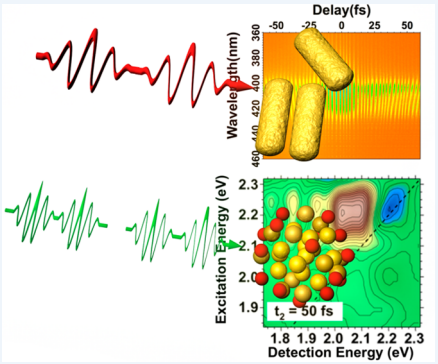

Based on these considerations, a detailed understanding of structure-dependent carrier dynamics across length scales requires an appropriate combination of spectroscopic methods. Plasmon mode-specific dynamics can be obtained through ultrafast correlated light and electron microscopy (UCLEM), which pairs interferometric nonlinear optical (INLO) with electron imaging methods. INLO yields nanostructure spectral resonance responses, which capture the system's homogeneous line width and coherence dynamics. State-resolved nanocluster dynamics can be obtained by pairing ultrafast with magnetic-optical spectroscopy methods. In particular, variable-temperature variable-field (VTVH) spectroscopies allow quantification of transient, excited states, providing quantification of important parameters such as spin and orbital angular momenta as well as the energy gaps that separate electronic fine structure states. Ultrafast two-dimensional electronic spectroscopy (2DES) can be used to understand how these details influence state-to-state carrier dynamics. In combination, VTVH and 2DES methods can provide chemists with detailed information regarding the structure-dependent and state-specific flow of energy through metal nanoclusters.

In this Account, we highlight recent advances toward understanding structure-dependent carrier dynamics for metals spanning the sub-nanometer to tens of nanometers length scale. We demonstrate the use of UCLEM methods for arresting interband scattering effects. For sub-nanometer thiol-protected nanoclusters, we discuss the effectiveness of VTVH for distinguishing state-specific radiative recombination originating from a gold core versus organometallic protecting layers. This state specificity is refined further using femtosecond 2DES and two-color methods to isolate so-called superatom state dynamics and vibrationally mediated spin-conversion and emission processes. Finally, we discuss prospects for merging VTVH and 2DES methods into a single platform.

1. INTRODUCTION

Throughout nature, simple rules yield complex, emergent phenomena. Nanomaterials exploit these rules to use electromagnetic radiation in novel ways. These unique opportunities arise because nanoscale-confined materials often display strikingly different chemical and physical properties than their bulk counterparts. In this Account, recent developments toward correlation of structure to optical and electronic properties for metal nanosystems are described. This information is a critical precursor to elucidate how these properties affect the function of these systems for photocatalysis, excited state-to-state energy transfer, and other photonic applications.

For metals, optical and electronic properties vary widely with size and shape (Figure 1). Discrete electronic excitation generates an exciton in nanoclusters (<2 nm), which can radiatively decay by emission of visible and near-infrared photons.[1] The emission yields of these systems are determined by nonradiative, vibrationally (or phonon) mediated electronic relaxation pathways on femtosecond to microsecond time scales.[2] In this metal size regime, electronic, and in turn optical, properties are not size scalable. Rather, they are defined by nanocluster structure (i.e., composition and symmetry). In contrast, the localized surface plasmon resonance (LSPR) of larger gold nanoparticles results from collective, phase-coherent excitation of conduction band electrons. LSPR excitation

Received: March 6, 2018
Published: May 8, 2018

DOI: 10.1021/acs.accounts.8b00096
Acc. Chem. Res. 2018, 51, 1433−1442

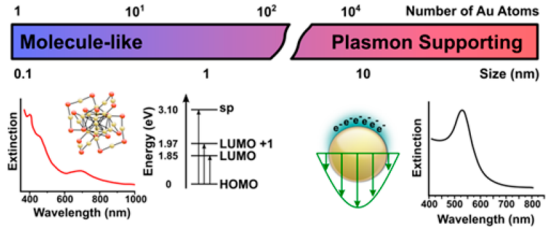

Figure 1. Size-dependent optical and electronic properties of metal nanoparticles.

produces large local surface fields at material-specific frequencies that selectively enhance optical signals.[3] LSPR enhancement factors and resonator frequencies can be tailored by strategic arrangement of metal nanoparticles into an electromagnetically coupled network.[4] The optical properties of these networks depend on interparticle plasmon-mode quality factors. This quality factor is determined by electronic coherence times for LSPR excitation, which typically persist for tens of femtoseconds.

Nanometals also exhibit catalytic properties. Plasmon-enhanced photocatalysis results when metal nanoparticles are interfaced with semiconductor materials.[5] The origin of this photocatalytic enhancement remains unresolved, but inclusion of metal nanoparticles likely has two main effects: improved charge injection and increased local electric fields.[6] Since these small nanoclusters cannot induce strong local electric fields, charge injection from excited charge carriers within the nanocluster may dominate. Understanding nanocluster and nanoparticle nonequilibrium carrier dynamics is an important step toward achieving a full understanding of photocatalysis involving metal-containing systems.

Comprehensive structure-dependent descriptions of nanometal carrier dynamics are critical for advancing nanoparticle-based applications. Major impediments to achieving these descriptions include the inherent heterogeneity of colloidal nanometals and the fundamentally different time scales for carrier dynamics in the ultrasmall nanocluster and larger nanoparticle domains. Insights into structure- and plasmon-mode-specific electronic dynamics have been obtained in our laboratory using ultrafast correlated light and electron microscopy (UCLEM).[7,8] This approach combines few-cycle femtosecond time-resolved interferometric nonlinear optical (NLO) imaging with scanning and transmission electron microscopy to obtain structure-specific resonance responses and electronic coherence dynamics of plasmon modes; both UCLEM components provide single-structure sensitivity. Monolayer-protected clusters (MPCs) represent an emerging class of nanomaterials for understanding properties of ultrasmall metal domains. Much like gas-phase clusters, specific "magic" sizes of MPCs can be isolated, owing to a combination of electronic and geometric shell closings.[9] This structural specificity facilities understanding structure−property relationships through ensemble measurements. We have used femtosecond two-dimensional electronic spectroscopy (2DES)[10] in combination with variable-temperature variable-magnetic-field (VTVH)[11,12] measurements to develop state-resolved carrier dynamics models for sub-nanometer gold nanoclusters. Whereas 2DES isolates excited-state-specific dynamics, VTVH quantifies electronic term symbols, state-specific electron-vibration (phonon) coupling strengths, fine-structure-state energy gaps, and spin assignments for these discrete transitions.

In the remainder of this Account, important advances toward a comprehensive understanding of nanogold carrier dynamics is given. In section 2, the use of UCLEM for elucidating plasmon-mode-specific coherence dynamics is demonstrated from research on single gold nanorods. In section 3, state-specific carrier dynamics of ultrasmall gold nanoclusters is discussed. As an example of state-resolved and structure-specific dynamics,

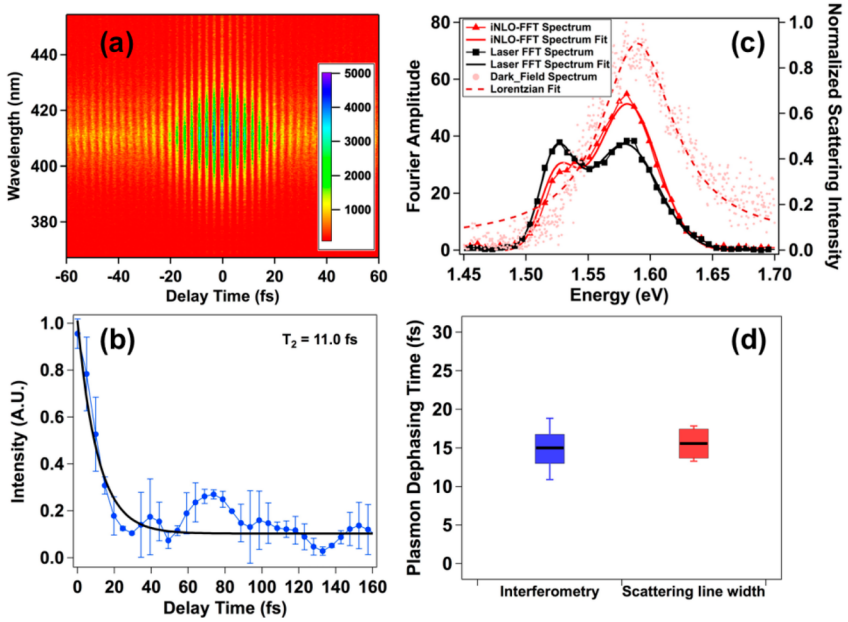

Figure 2. Summary of spectral interferometric NLO (INLO) analysis. (a) INLO map from a gold-nanosphere homodimer obtained by plotting wavelength-resolved SHG versus interpulse time delay. (b) Time-dependent SHG amplitude (filled blue ●) and fit (black) extracted from panel a as described in the text. (c) Overlay of single-nanostructure (LSPR = 1.59 eV) INLO FFT, laser fundamental (black square), and dark-field scattering (DFS) spectra. (d) Dephasing time comparison determined from INLO and DFS line widths, averaged over several single-structure measurements. Reproduced with permission from refs 7 and 8. Copyright 2015, 2016 American Chemical Society.

DOI: 10.1021/acs.accounts.8b00096
Acc. Chem. Res. 2018, 51, 1433−1442

2DES is applied to isolate valence and conduction band dynamics for neutral and anionic $Au_{25}(SC_8H_9)_{18}^{0/-}$ nanoclusters. In combination with VTVH, ultrafast spectroscopy reveals how electronic-state-specific coupling to low-frequency vibrational modes mediates carrier dynamics for nanoclusters. In section 4, concluding remarks and outlooks, including prospects for merging 2DES and VTVH into a single platform, are given.

2. PLASMON QUALITY FACTORS FROM UCLEM

The efficiency of plasmon amplification depends on mode quality factor, which is related to electronic coherence time; persistent coherence yields greater amplification efficiency.[7] Primary decoherence mechanisms for gold nanoparticles include interband scattering, interfacial and intrinsic damping, and radiative decay.[13] The effect of interband scattering is discussed herein. Femtosecond time-resolved interferometric imaging techniques based on nonlinear optical (INLO) signals are effective for providing mode-specific plasmon coherence times.[7,8] These measurements provide both the plasmon-resonance response for many INLO signals and the associated ~10 fs electronic dephasing (coherence) time.

An example of a frequency-resolved, second-harmonic-generation (SHG)-detected interferogram from a single gold nanosphere dimer is given in Figure 2a. The interferogram is generated using a sequence of phase-stabilized femtosecond pulse replicas, which are temporally delayed on the attosecond to femtosecond time scales. After the nonresonant SHG instrument and sample resonance responses have been determined, time-resolved data resulting from plasmon-resonant excitation of the nanostructure can be extracted (Figure 2b). This is accomplished by determining the time-dependent optical response of a system, $P(t)$, which describes the interaction between a stimulating optical field and the material.[7] For a nonresonant nonlinear medium, an instantaneous response proportional to the laser electric field, $E(t)$, gated by the time-delayed pulse $E(t - t')$, is measured. If the sample is resonant within the excitation bandwidth, as is the case for plasmon-mediated excitation, the finite response time leads to an induced polarization transient, $P(t)$, and the output signal is a convolution of the driving laser pulse, $E(t)$, and the sample resonance response function, $R(t)$, given by

$$P(t) = E(t) \otimes R(t) = \int R(t - t')E(t')\, dt' \quad (1)$$

$R(t)$ is modeled as a damped harmonic oscillator in the time domain,

$$R(t) = A \exp(i\omega_{LSPR}t - \gamma t) \quad (2)$$

where A gives the effective oscillator strength, ω_{LSPR} is the plasmon resonance frequency, and γ is the line width described by $\gamma = 1/T$, where T is the plasmon coherence dephasing time. It is important to appreciate that at the single-particle measurement level, γ represents a homogeneous line width for an electronic (i.e., plasmonic) transition, and hence, T reports structure- and mode-specific carrier dynamics.

INLO accuracy for capturing plasmon dephasing dynamics for single nanorods is illustrated in Figures 2c,d. The Figure 2c spectra were obtained by Fourier transformation of time-domain interferometric data.[8] The black Fourier spectrum shows the double-Gaussian profile of the laser pulse, whereas the red trace shows the increased signal amplitude at 1.59 eV originating from resonant-LSPR nanorod excitation. The plasmon-dephasing time was retrieved by deconvolution of fundamental (black squares) and INLO signals (red triangles). INLO responses are compared to dark-field scattering (DFS) line width results in Figure 2d. Averaging over multiple nanorods, dephasing time constants of 15 ± 4 fs and 16 ± 2 fs resulted from interferometric (blue) and DFS line widths (red), respectively. The excellent agreement between these results confirms INLO reliability for resolving single-structure electronic dynamics, opposed to surface field decay.

Using these methods, nanorod length-to-diameter aspect-ratio-dependent trends in plasmon coherence dynamics were determined.[8] DFS spectra for three different model aspect ratios (ARs) 1.86 (blue), 2.91 (black), and 3.90 AR (red), with LSPR energies of 2.06, 1.77, and 1.55 eV, respectively,[8] are overlaid in Figure 3a. Figure 3b–d shows corresponding

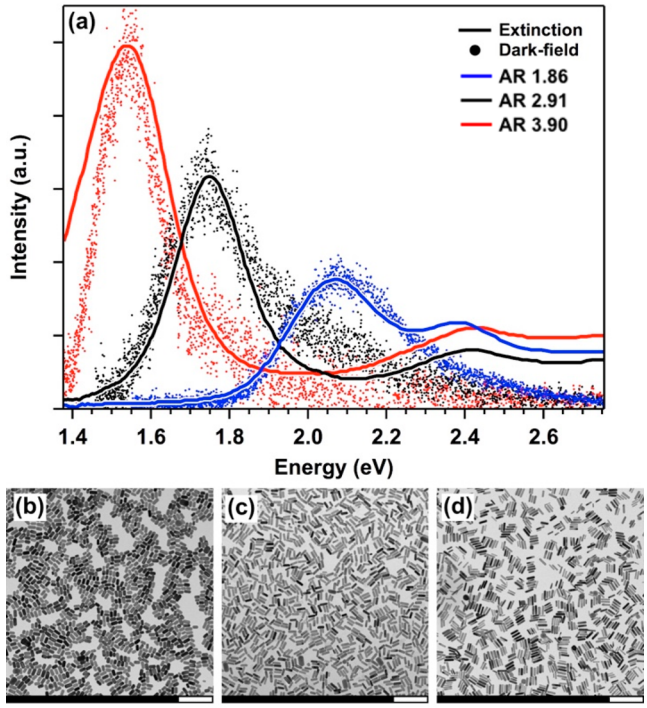

Figure 3. (a) Ensemble extinction (solid lines) and single-particle DFS spectra (filled circles) for 1.86 (blue), 2.91 (black), and 3.90 AR (red) nanorods. TEM images for 1.86 (b), 2.91 (c), and 3.90 AR nanorods (d). Scale bars represent 200 nm. Reproduced with permission from ref 8. Copyright 2016 American Chemical Society.

electron microscope images. The relative contributions of plasmon-dephasing processes are volume dependent. Therefore, isolation of structure-specific dynamics requires comparison of constant-volume samples. These studies isolate the influence of interband scattering on plasmon coherence. Coherent intraband electron scattering with the interband transition is a significant plasmon dephasing mechanism, and rod lengthening allows for energetic decoupling of the plasmon (intraband) excitation from the interband transition.[13,14] Hence, plasmon coherence times should be extended as the length-to-diameter aspect ratio increases. INLO clearly resolves this effect.

Figure 4 (panel a, AR = 2.91; panel b, AR = 3.90) compares single-nanorod INLO-detected and laser fundamental spectra. The nanorod spectrum gives the resonance response, from which the homogeneous line width is determined. Electronic

DOI: 10.1021/acs.accounts.8b00096
Acc. Chem. Res. 2018, 51, 1433–1442

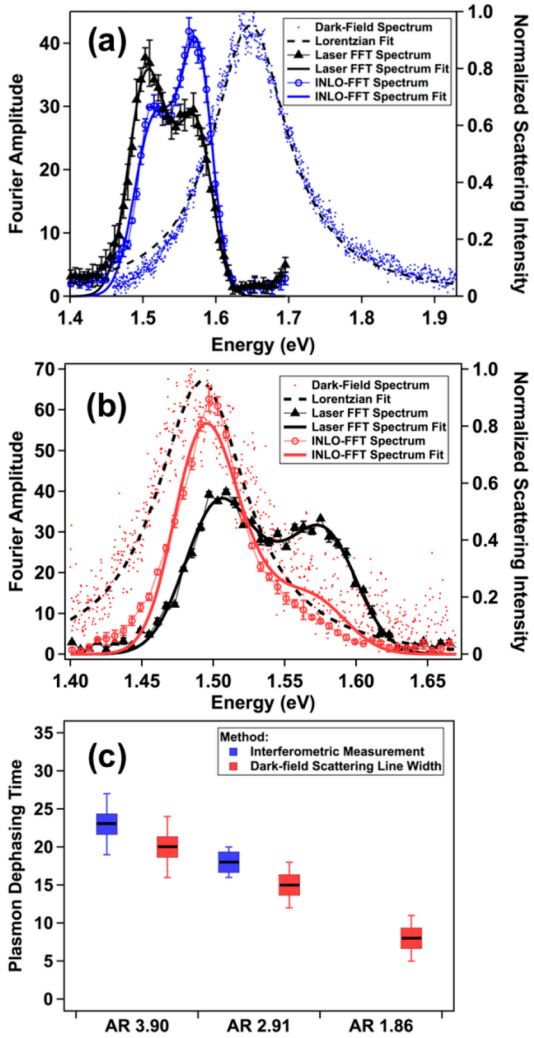

Figure 4. Comparison of DFS and INLO spectra for (a) length-to-diameter AR = 2.91 and (b) AR = 3.90 gold nanorods, measured at the single-particle level. (c) Summary of plasmon dephasing (coherence) time for AR = 1.86, 2.91, and 3.90 nanorods. The trend to longer coherence time with increased AR reflects the suppression of plasmon dephasing via interband scattering channels. Reproduced with permission from ref 8. Copyright 2016 American Chemical Society.

coherence times were also retrieved by DFS. Figure 4c compares average dephasing times extracted from INLO and DFS measurements for several nanorods. The INLO-determined dephasing times are 23 ± 4 fs (AR 3.90) and 18 ± 2 fs (AR 2.91). DFS measurements show 20 ± 4 fs (AR 3.90) and 15 ± 3 fs (AR 1.86) dephasing times. AR 1.86 AuNRs have an 8 ± 3 fs dephasing time; INLO was not used for this sample due to lack of spectral overlap between plasmon and excitation resonance energies. Both methods show the same trend; coherence time increases when the length-to-diameter AR is made larger. The associated plasmon quality factors are 7 (AR 1.86), 11 (AR 2.91), and 18 (AR 3.90). This increase results from detuning of the coherent LSPR and interband transition energies for larger AR.[8,14]

The nanorod studies demonstrate how UCLEM informs on structure-dependent nanoscale optical properties and carrier dynamics. In this specific case, modifying the nanostructure aspect ratio results in an ~3× increase in plasmon coherence time and, as a result, mode quality factors. This optimization results because nanoparticle dimensions, which can be tailored by colloidal synthesis, can be used to modify resonance energies for specific plasmon modes. These results make clear the necessity to account for fundamental carrier dynamics when developing applications featuring nanostructures as functional components.

Proposals to extend plasmon coherence times include incorporation of nonradiative modes within hybridized interparticle resonances of multiparticle assemblies. This hybridization scheme has the effect of suppressing radiative plasmon dephasing by coherent interference between "bright" dipolar and "dark" high-order modes.[15] Therefore, hybridized interparticle plasmons may be treated analogously to state-specific molecular dynamics, where mode angular momentum determines electronic coherence of the nanostructure. Hybridization models based on molecular orbital theories have effectively predicted the steady-state optical properties of coupled metal nanoparticles, but by comparison, little is known about time-dependent coherent electron dynamics of nanoparticle assemblies. The single-particle INLO methods described in this Account are ideally suited to provide this understanding because Fourier analysis resolves the homogeneous line widths of both radiant and nonradiant modes.

Plasmon-based electromagnetic transduction provides many opportunities for chemists to manipulate and control energy at the nanoscale. Improving mode quality factors or persistent coherence times of isolated nanoparticles that form arrays is a critical first step for structure optimization. The amplitude and frequency of coherent interparticle resonances can be tuned by adjusting dimensions of nanoparticle building blocks that form assemblies, as well as their relative orientations and interparticle spatial separations. Thus, nanoparticle structure can be used to control the coherent plasmon dynamics and optical properties of these systems. Dissecting the details of this structure–photonic-property interplay requires experimental methods like UCLEM. Important new insights will be gained if the UCLEM approach is expanded to include 3-D transmission electron tomography (TET). 3-D TET allowed us to resolve interfacial structures in networks of hollow gold nanospheres (HGNs).[16] Hybridized plasmon resonance energies, and the associated mode quality factors, of these systems depend dramatically on details of interparticle structure. Predictive design of functional plasmonics will require the level of structural detail available from UCLEM tomography measurements.

3. STATE-RESOLVED DYNAMICS IN MONOLAYER-PROTECTED CLUSTERS

A key optical feature of ultrasmall gold domains is photoluminescence emission. In contrast to the rapid radiative decay of plasmonic nanoparticles (section 2), emission lifetimes for sub- to few nanometer gold nanoclusters can extend to microseconds.[2,10] Photoluminescence mechanisms for these systems have been widely debated, invoking both ligand-to-metal charge-transfer processes and metal-centered intraband radiative decay.[18,19] Using a combination of state-resolved variable-temperature variable-field magnetic-circular photoluminescence (VTVH-MCPL) and ultrafast 2D-electronic spectroscopy (2DES) techniques, which collectively span the tens of femtoseconds to hundreds of microseconds time scales, our group has found experimental evidence suggesting both mechanisms contribute to nanocluster emission.[11] Specifically, nanocluster emission yields are determined by state-specific and vibration-mediated dynamics of discrete electronic car-

DOI: 10.1021/acs.accounts.8b00096
Acc. Chem. Res. 2018, 51, 1433−1442

riers.[11,12,17] Select examples from VTVH-MCPL and 2DES examinations that allow determination of structure-specific and state-resolved electron dynamics for gold monolayer-protected clusters (MPCs) are summarized.

The emergence of colloidal MPCs as structurally precise model systems allows new opportunities for describing state-resolved dynamics for sub- to few nanometer metals. Using $Au_{25}(SC_8H_9)_{18}^-$ as a prototype (Figure 5), MPCs include three

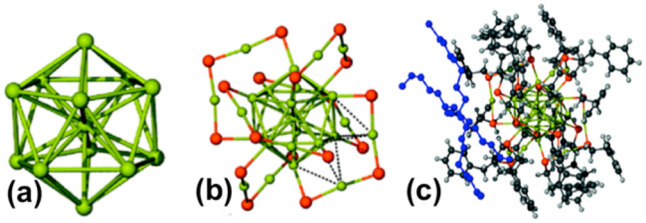

Figure 5. Overview of three structural components forming $Au_{25}(SC_8H_9)_{18}^-$ monolayer-protected clusters (MPCs), including (a) 13-atom gold core, (b) six gold–sulfur protecting units, and (c) organic passivating ligands with counterion (blue). This three-domain structure is general to many MPC sizes. Each component influences MPC photonic properties.

distinguishable structural domains: (a) metal cluster cores; (b) inorganic (e.g., alternating Au–S) staple motifs that "protect" the central core; and (c) passivation ligands that facilitate MPC solution dispersion.[9] Spectroscopic methods that can address the influence of each MPC domain on photonic properties are necessary for establishing structure–function relationships for these materials.

The pronounced stability of "magic" MPC sizes results from a combination of valence electron configuration and steric interactions in the organometallic/ligand shell. Superatom models describe the stationary-state electronic structure of $Au_{25}(SC_8H_9)_{18}^-$. The valence electrons of the metal atoms are delocalized throughout the entire nanocluster core.[9,20,21] For a spherical system, the orbitals then adopt 1S, 1P, 1D, 2S, 1F, 2P, etc. symmetries. The number of delocalized electrons, n, in the nanocluster with stoichiometry $M_NX_Y^z$ (M = metal atoms; Y = one-electron-withdrawing or -localizing ligand; z = oxidation state) is determined by $n = N - Y - z$, where N is the number of valence electrons contributed by the metal atoms. If n corresponds to a spherical magic number (2, 8, 18, 34, 58, etc.), the nanoparticle may be stable. $Au_{25}(SC_8H_9)_{18}^-$ corresponds to an 8-electron ($1S^21P^6$) system with superatom P HOMO and D LUMO manifolds. Further, the delocalized core orbitals experience ligand-field splitting from surrounding ligands, which affects the ordering and energy separations between fine-structure components of these states.[21]

The influence of these structural and electronic effects on $Au_{25}(SC_8H_9)_{18}$ PL yields has been determined from VTVH-MCPL and temperature-dependent, intensity-integrated PL studies.[11,12] The 4.5 K PL spectrum of $Au_{25}(PET)_{18}$ (3.1 eV excitation) is shown in Figure 6. The global PL includes multiple components. An advantage of MCPL spectroscopy is the ability to resolve spectrally congested components through polarization-dependent detection. MCPL spectra plot the intensity differences between left and right circularly polarized emission, which originate from distinct electronic spin states. The 4.5 K PL and MCPL spectra are overlaid in Figure 6. From this comparison, it is clear that $Au_{25}(SC_8H_9)_{18}$ emission

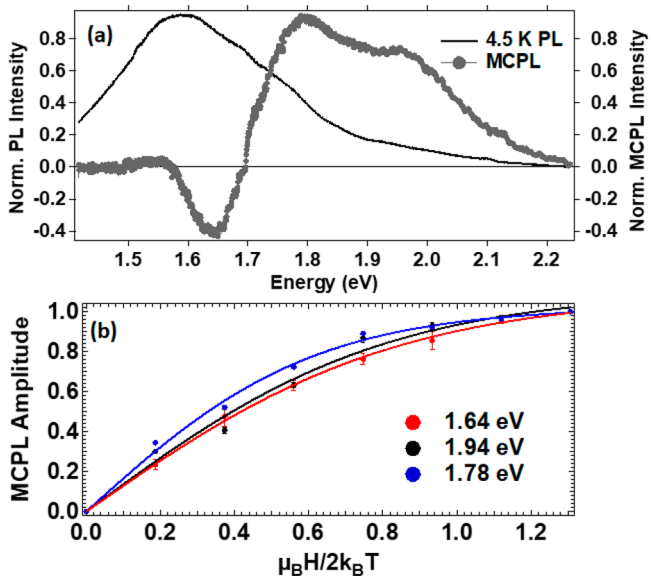

Figure 6. (a) $Au_{25}(SC_8H_9)_{18}$ photoluminescence spectrum at 4.5 K (black), following 3.1 eV excitation. Representative differential MCPL spectrum generated from PL collected at ±17.5 T (gray). (b) Differential peak amplitudes plotted vs applied field strength at constant sample temperature (4.5 K); data correspond as follows: 1.64 eV (red), 1.78 eV (blue), and 1.94 eV (black). Reproduced with permission from ref 12. Copyright 2017 Optical Society of America.

includes three distinguishable components with mean energies of 1.64, 1.78, and 1.94 eV.

Using VTVH-MCPL, spectroscopic term symbols, which contain state-specific spin- and orbital-angular momenta quantization, are assigned to each $Au_{25}(SC_8H_9)_{18}$ emission component.[12] These assignments are a first step in understanding state-resolved carrier dynamics. Term symbols are determined from Landé g-factors, which provide quantitative representation of the total angular momentum for spin–orbit coupled (SOC) electronic states. Landé g-factors are quantified through analysis of differential peak amplitudes versus applied-field strength ($\vec{H}$) and sample temperature (T):

$$\Delta I = A_{sat} \tanh\left(\frac{g\mu_B\vec{H}}{2k_BT}\right) \quad (3)$$

A_{sat} is the saturation amplitude, g is the Landé g-factor, μ_B is the Bohr magneton, and k_B is Boltzmann's constant. Field-dependent amplitudes for each component are shown in Figure 6b. Fits to these data yield g-factors of 1.1 ± 0.1 (1.64 eV), 1.6 ± 0.1 (1.78 eV), and 1.05 ± 0.04 (1.94 eV). Considering SOC, D-doublet terms were determined for the 1.64 and 1.94 eV transitions. The 1.78 eV component was assigned as P-quartet. An important outcome of these studies is the direct experimental evidence of radiative recombination via excited superatom (D) states. Whereas, steady-state MCD measurements detail ground-state electronic structure, MCPL methods report on transient excited states. To summarize MCPL assignments, the 1.64 and 1.94 eV transitions result from superatom D state dynamics. The 1.78 eV peak is tentatively associated with p orbitals of the organometallic band.[12]

The role of state specificity can be further dissected through temperature-dependent MCPL analysis, which quantifies energy separation between states and relative Faraday-term

DOI: 10.1021/acs.accounts.8b00096
Acc. Chem. Res. 2018, 51, 1433–1442

contributions to the differential response. Boltzmann distributed populations of occupied electronic states separated by $\sim k_B T$ are subject to variable thermal effects. At 4.5 K, only the lowest-energy levels are populated. Temperature-dependent population distributions reflect energy separations between fine-structure states. Under these conditions, MCPL responses can include *A*, *B*, and *C*, Faraday terms; *A* terms result from Zeeman splitting of unoccupied states, *B* terms are from field-induced mixing of electronic states, and *C* terms describe Zeeman splitting in occupied levels. For cryogenic measurements on paramagnetic systems (e.g., $Au_{25}(SC_8H_9)_{18}$), *C* and *B* terms are most significant. Equations 4 and 5 quantify the temperature-dependent MCPL response.

$$\text{amplitude} = \sum_i \left(\frac{C_i}{k_B T} \alpha_i \vec{H} + B_i \alpha_i \vec{H} \right) \tag{4}$$

$$\alpha_1 = \frac{1}{1 + e^{-\Delta/(k_B T)}} \tag{5}$$

C_i and B_i denote weighting factors for *C*- and *B*-terms, respectively, and α_i describes Boltzmann populations for each component. For each α, Δ denotes the energy separation between states. Figure 7 shows the temperature-dependent MCPL amplitudes for each component. The Δ values for the 1.64, 1.78, and 1.94 eV transitions are 3.8 ± 0.1, 0.42 ± 0.02, and 0.32 ± 0.05 meV, respectively.[12] The corresponding *C*-term amplitudes are 0.97 ± 0.01 (1.64 eV), 0.83 ± 0.02 (1.78 eV), and 0.94 ± 0.01 (1.94 eV).[12]

The VTVH-MCPL data provides a key new insight into state-specific nanocluster emission. The 1.64 eV peak results from nearly exclusive radiative recombination via superatom D orbitals (Δ = 3.8 meV; C term weight = 97%), whereas components detected at higher emission energies proceed by a manifold of nearly degenerate electronic states. A further distinguishing factor is that these recombination pathways are determined by state-specific electron−phonon coupling processes. Analysis of temperature-dependent emission energies for each component shows the 1.64 eV peak is coupled to low-frequency Au−Au vibrations, whereas the two higher-energy components couple to Au−S stretching modes, associated with the inorganic protecting layer.[17] Taken together, the assignments of spectroscopic term symbols, zero field splitting (ZFS), relative Faraday contributions, and electron−vibrational coupling, all of which are provided by VTVH spectroscopy, facilitate rich descriptions of nanocluster carrier dynamics. Specifically, the 1.64 eV peak results from superatom $^2D \rightarrow {}^2P$ recombination.[12] The 1.78 eV component results from emission involving p orbitals in the $(Au_2S_3)_6$ layers, and the 1.94 eV peak is attributed to superatom D state electron recombination with holes of the inorganic protecting motif.[12]

An important challenge is to address to what extent state-specific dynamics influence nanocluster optical properties. Indeed, $Au_{25}(SC_8H_9)_{18}$ emission yields depend on the relative amplitudes of specific emission components. Figure 8 shows temperature-dependent integrated global PL intensities for the MPC. An approximate 30% increase in PL intensity is observed upon raising the sample temperature from 4.5 to 50 K; reduced emission intensity results from further temperature increases.[17] These temperature-dependent intensity trends track branching ratios for the 1.64 and 1.78 eV peaks. Increased emission results when the 1.64 eV component dominates emission. These trends suggest Au−Au modes actually facilitate radiative recombination for core-based transitions, whereas activation of Au−S stretching results in preferential nonradiative decay for dynamics involving the inorganic protecting component.[17] These results are encouraging because they suggest structural modifications to specific MPC structural motifs may allow tailoring of nanocluster optical properties. But, predictive design of nanocluster properties requires state-specific descriptions of how vibrational coupling influences carrier dynamics.

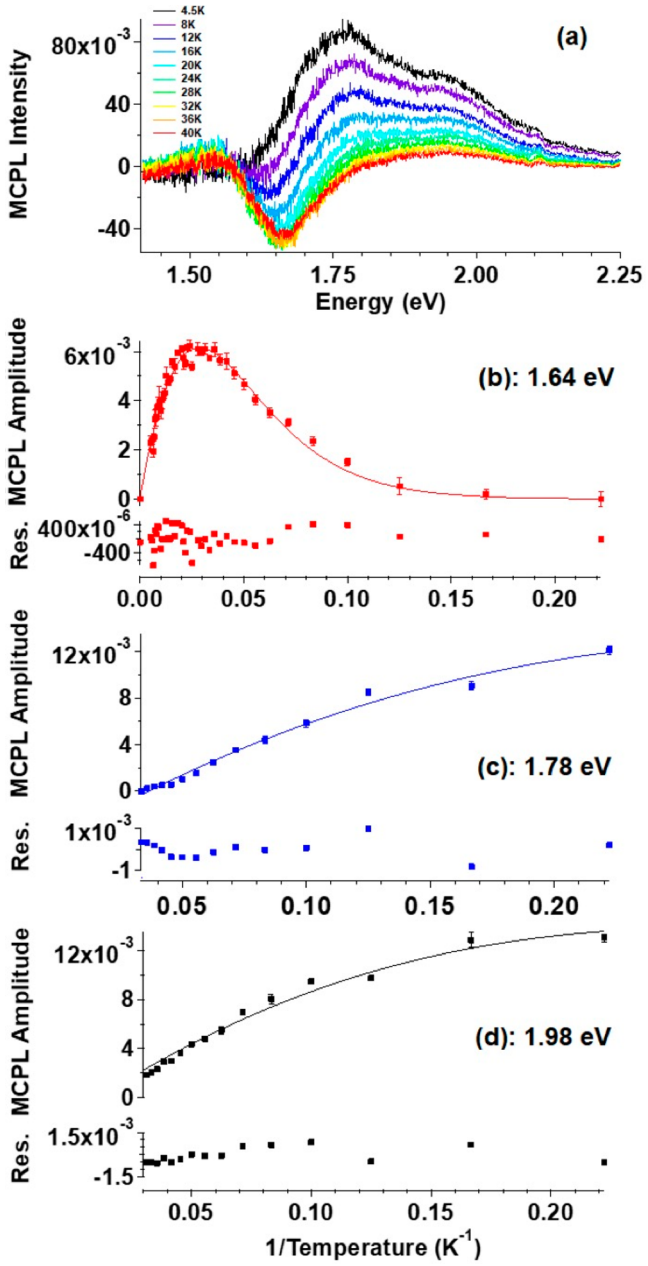

Figure 7. (a) Temperature-dependent MCPL spectra acquired from 4.5 to 40 K in 4 K steps using ±17.5 T applied field strength. (b−d) Resultant VT-MCPL amplitudes for each peak with fit residuals. Reproduced with permission from ref 12. Copyright 2017 Optical Society of America.

In order to obtain state-to-state carrier dynamics, we have examined MPCs using ultrafast 2DES.[10] The multidimensional spectroscopy approach preserves the high temporal resolution of ultrafast spectroscopy, while providing state-resolved

DOI: 10.1021/acs.accounts.8b00096
Acc. Chem. Res. 2018, 51, 1433−1442

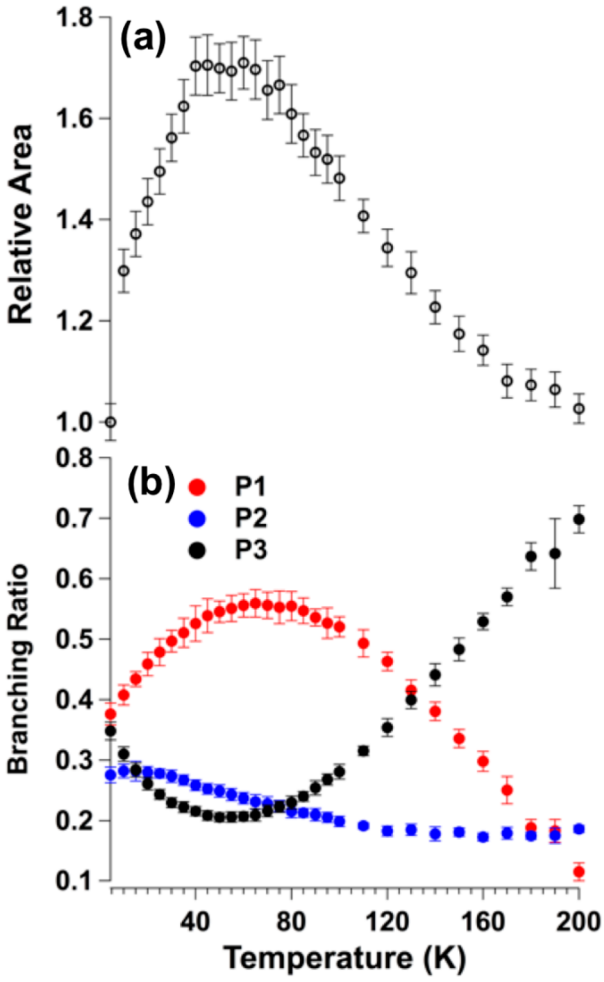

Figure 8. (a) Integrated intensity of $Au_{25}(SC_8H_9)_{18}$ photoluminescence plotted versus temperature, normalized at 4.5 K. Increased temperature (4.5−50 K) leads to greater emission. Elevating sample temperature from 50 to 200 K results in reduced photoluminescence. (b) Temperature-dependent branching ratios of three $Au_{25}(SC_8H_9)_{18}$ emission components, where P1 and P3 correspond to the 1.64 and 1.78 eV components, respectively. Correlation between P1 and P3 branching ratios and integrated-photoluminescence yields is observed. Reproduced with permission from ref 17. Copyright 2014 American Chemical Society.

dynamics by spreading transient signal amplitudes over both excitation and detection axes. 2DES studies in our group have focused on core-based electronic transitions within the manifold of states near the HOMO−LUMO gap of $Au_{25}(SC_8H_9)_{18}$. 2DES studies have revealed internal conversion and intramolecular vibration redistribution dynamics of carriers in both the superatom P and D states.

Figure 9 shows a series of 2D-absorption plots for $Au_{25}(SC_8H_9)_{18}^-$ at designated pump−probe delay times. For 1.95 eV excitation, a single excited-state absorption (ESA) peak is detected with mean energy of 2.05 eV for all given waiting times. The 1.95 eV excitation promotes an electron from the superatom P to D manifold, corresponding to LUMO + 1; LUMO ← HOMO − 1; HOMO − 2 transitions. For 2.21 eV excitation, several ESA features are detected at early waiting times, <100 fs. At longer time delays, the ESA features merge into a single peak, which exhibits a time-dependent shift to higher detection energy. This energetic shift results from electronic internal conversion within the superatom D

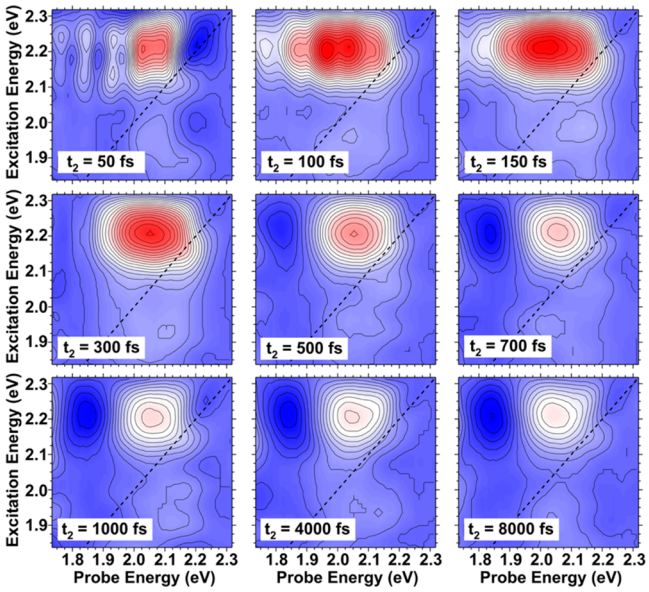

Figure 9. 2DES plots at designated population times. Red represents negative $\Delta T/T$ due to excited-state absorption and blue (positive) signifies transient bleaching. Reproduced with permission from ref 10. Copyright 2016 American Chemical Society.

manifold, requiring more energetic photons to access a continuum final state in the probe step. In contrast, 1.95 eV excitation promotes the electron directly to the nearly degenerate LUMO and LUMO + 1 superatom D states. As a result, an ESA energy shift is not observed within the several picosecond time scale. The 1.95 eV cross peaks are amplified 4× in Figure 10a,b for reference.

Because 2DES allows analysis of select excitation/detection energy combinations, carrier dynamics for specific excited states can be examined. Figure 10 shows the recovery dynamics taken at 1.95 and 2.21 eV excitation within the ESA signal region. The

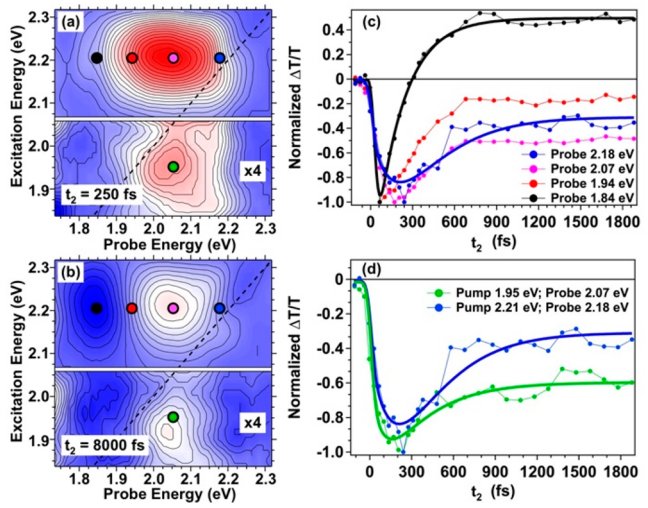

Figure 10. (a,b) 2DES maps with the region from 1.73 to 2.07 eV multiplied by 4× to emphasize the low-pump-energy cross peak. (c,d) Extracted pump−probe dynamics from regions identified by colored markers in panels a and b. Panel c data resulted from 2.21 eV excitation. Solid lines are double exponential fits convolved with a Gaussian instrument response. Reproduced with permission from ref 10. Copyright 2016 American Chemical Society.

DOI: 10.1021/acs.accounts.8b00096
Acc. Chem. Res. 2018, 51, 1433−1442

dynamics were fit with an exponential growth and decay function to recover the time constants. The 1.95 eV/2.07 eV excitation/detection dynamics revealed an accelerated growth time constant of 85 ± 15 fs compared to 200 ± 15 fs for 2.21 eV/2.18 eV. The recovery time constant of 310 ± 35 fs for both excitation/detection traces agreed within error. These selective excitation/probe results allowed isolation of superatom D electron dynamics from superatom P hole. Electrons internally convert within the superatom D manifold in ~200 fs and holes thermalize the superatom P in ~300 fs, depicted in Figure 11.

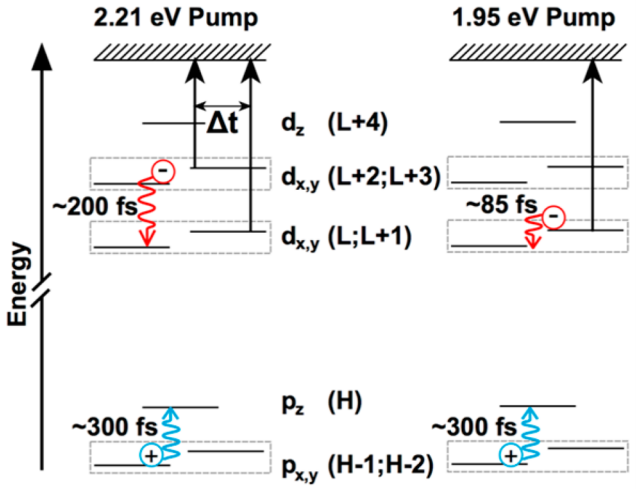

Figure 11. Model describing relaxation dynamics of electrons and holes following 2.21 eV (left) and 1.95 eV excitation (right). Reproduced with permission from ref 10. Copyright 2016 American Chemical Society.

This result is the first sub-100 fs resolved description of superatom state dynamics for any MPC. In future research, 2DES can provide an important experimental tool to investigate how MPC structural modification affects state-specific carrier dynamics.

We have extended MPC structure and state-specific dynamics studies using two-color (visible pump/near-infrared (NIR) probe) ultrafast spectroscopy.[22] By focusing on transiently excited states near the $Au_{25}(SC_8H_9)_{18}^0$ HOMO–LUMO energy gap, we detected a previously unobserved few-hundred picoseconds relaxation channel. Spectrally resolved measurements revealed an energetic barrier that influenced this relaxation rate constant (Figure 12). Interestingly, this effect was oxidation-state dependent. Generally, we attributed these dynamics to relaxation through a manifold of states, but we postulated that unpaired electrons could play a role in the observed oxidation-state dependence; the anion corresponds to a filled superatom orbital, whereas the neutral does not. Further studies are necessary, but one possible explanation for the oxidation-state-specific carrier dynamics involves vibrationally mediated intersystem crossing processes. These findings suggest that straightforward chemical modifications can lead to substantially different relaxation dynamics and optical properties for MPCs. This level of control and tunability is unusual for colloidal nanoparticles.

Both PL and ultrafast spectroscopy point to the importance of electron–vibration coupling for determining MPC carrier dynamics. Vibrational influence can be obtained from 2DES data.[9] For example, the 1.95 eV/2.05 eV cross peak exhibits

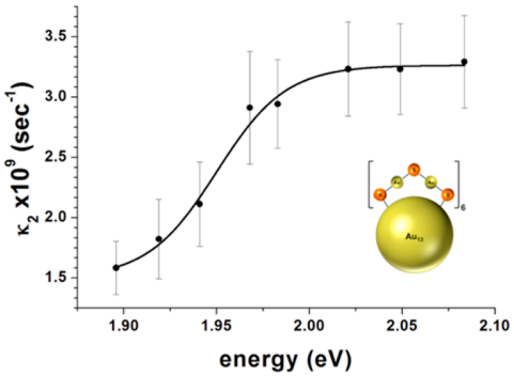

Figure 12. Relaxation rate-constant summary obtained for $[Au_{25}(SR)_{18}]^0$ nanoclusters. The data reflect an energy barrier at approximately 100 meV above the 1.85 eV HOMO–LUMO energy gap. Reproduced with permission from ref 22. Copyright 2012 Royal Society of Chemistry.

periodic time-dependent detection-energy modulations. Fourier transformation of these time-domain data yields a low-frequency mode, which is consistent with Au–Au vibrations. Therefore, these 2DES results are consistent with MCPL data that implicate Au–Au dilation modes for mediating core-based luminescence. In fact, these periodic oscillations are ubiquitous in MPC ultrafast data.[23] A select summary is given for $Au_{25}(SC_8H_9)_{18}^-$ and $Au_{144}(SC_8H_9)_{60}$ in Figure 13. The $Au_{144}(SC_8H_9)_{60}$ results are especially interesting because they reveal multiple vibrational modes for different excitation/detection energies. Shown in Figure 13d, both Au–Au core-based (1.4 THz) and Au–S modes of the inorganic protecting component (2.0 THz) can be isolated from selective correlation of excitation and detection energies.

It is important to appreciate that the vibrational modes observed in the ultrafast experiments also affect state-specific emission yields for MPCs. By combining ultrafast 2DES with VTVH methods, it is possible to span the relevant time scales for nanocluster carrier dynamics and obtain descriptions of how state-resolved dynamics determine the optical properties of these systems. Future research that pairs these two spectroscopic approaches is poised to provide key insights into structure-specific descriptions for nanoparticle optical and electronic properties.

An important aim of fundamental metal nanoparticle research is to understand domains spanning the range of 1–3 nm, where the transition from discrete to collective electronic behavior is expected to occur. MPCs allow new opportunities in this area. Using ultrafast spectroscopy, we have surveyed a series of clusters spanning as few as 20 gold atoms (<1 nm diameter) to as many as 460 atoms (2.5 nm diameter), allowing us comprehensive examination of electronic relaxation dynamics of gold nanoscale domains.[2] Our femtosecond transient spectroscopy reveals that the $Au_{144}(SR)_{60}$ system is the smallest identifiable metallic species.[2,24] However, it is important to note that for these ultrasmall gold systems, optical and electronic properties are not necessarily expected to be size scalable. Therefore, there is perhaps not an abrupt "magic size" for which the onset of metallic or collective electronic behavior should be observed. Rather, systematic studies of how geometric structure and composition influences the fundamental properties of these systems are needed. To this end, we have used the 144-atom cluster as a model for understanding how the formation of bimetallic Au–Ag species affects electron–

DOI: 10.1021/acs.accounts.8b00096
Acc. Chem. Res. 2018, 51, 1433–1442

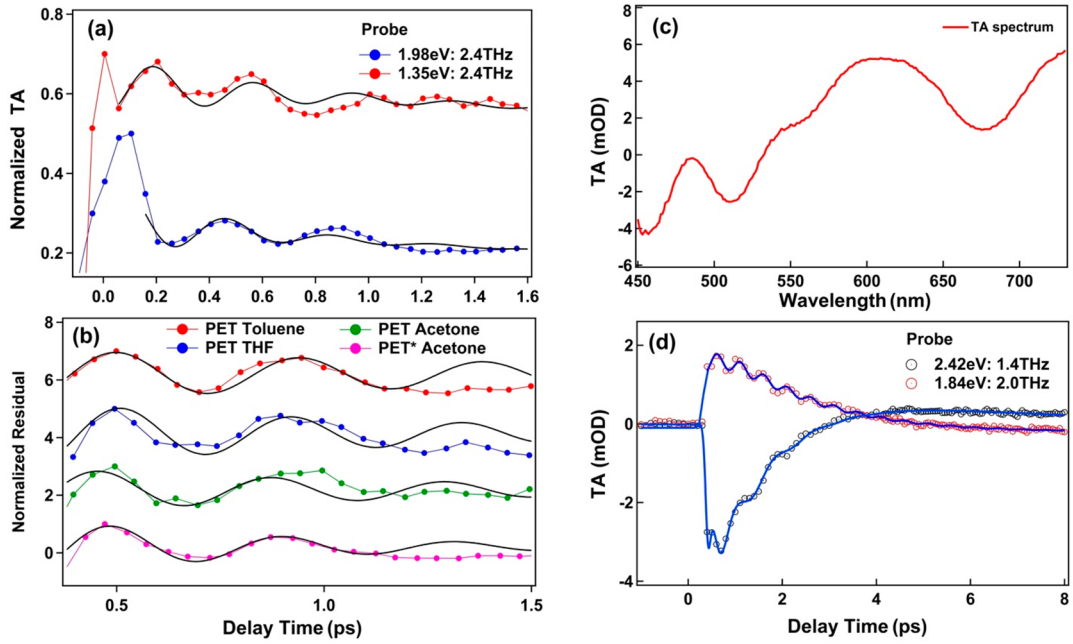

Figure 13. Detection of coherent modes for $Au_{25}(SC_8H_9)_{18}^-$ (a,b) and $Au_{144}(SC_8H_9)_{60}$ (c,d). $Au_{25}(SC_8H_9)_{18}^-$ vibrations are detected only at specific excitation/detection energy combinations. This finding suggests that MPCs exhibit state-specific electronic-relaxation dynamics. State-selective probing reveals two distinct $Au_{144}(SC_8H_9)_{60}$ vibrational modes (d). Panels a and b reproduced with permission from ref 23. Copyright 2017 American Chemical Society.

phonon coupling and energy dissipation.[25] These results showed a clear trend in metal composition on electron−phonon coupling and also indicated silver atom substitution of gold occurs preferentially at the metal cluster core of the MPC. In this way, structurally well-defined MPCs can be used to refine our understanding of the structure−property interplay on the nanoscale.

4. CONCLUSIONS AND OUTLOOK

Structure-specific and state-resolved electronic carrier dynamics and optical properties for a comprehensive range of metal nanoparticles have been described. For plasmonic nanoparticles, UCLEM allows examination of plasmon coherence dynamics for collective resonances. These coherence times can be manipulated by the relative arrangement of nanoparticles within a network. This structural dependence is important to understand because plasmon amplification and optical sensing applications can all be improved by increased mode coherence times.

For MPCs, vibrationally mediated state-resolved dynamics were obtained from a combination of ultrafast 2DES and VTVH-MCPL spectroscopy studies. This powerful approach describes carrier dynamics in greater detail than could be achieved using either method alone. VTVH-MCPL allows assignments of excited emissive states, including description of orbital angular and spin momenta (term symbols), as well as fine-structure state ZFS energies. The ZFS and term information can be used to understand how MPC chemical composition and size influence geometric and electronic structure. Both VTVH and 2DES experiments highlight the important role of low-frequency vibrations on nanocluster carrier dynamics. VTVH-MCPL data show that nanocluster emission yields are directly influenced by the nature of how carriers couple to vibrational modes for specific excited states. Results presented here demonstrated Au−Au vibration-enhanced PL for radiative recombination by MPC superatom states, whereas Au−S vibrations reduced emission yields for states associated with the nanocluster organometallic motif. Ultrafast spectroscopy completes the view of electronic dynamics by isolating specific carriers and capturing how vibrational modes influence processes like intersystem crossing and internal conversion.

Future research that pairs the information content of VTVH and 2DES methods into a single experimental platform could be transformative in understanding nanoscale cluster dynamics. In tandem, VTVH-2DES could provide state assignments for transiently excited states that mediate nanoscale energy relaxation. VTVH methodology should be insightful for most spin−orbit coupled materials, extending the range of studies presented here beyond nanometals.

AUTHOR INFORMATION

Corresponding Author

*E-mail: klk260@psu.edu.

ORCID

Kenneth L. Knappenberger Jr.: 0000-0003-4123-3663

Funding

Portions of this work were supported by grants from the Air Force Office of Scientific Research (FA9550-15-1-0114) and the National Science Foundation (CHE-1507550 and CHE-110249).

Notes

The authors declare no competing financial interest.

Biographies

Tian Zhao earned his M.S. in Chemistry from Beihang University and is currently a doctoral student at Pennsylvania State University. His research interests include ultrafast correlated light and electron microscopy and plasmonics.

DOI: 10.1021/acs.accounts.8b00096
Acc. Chem. Res. 2018, 51, 1433−1442

Patrick Herbert earned his M.S. at Florida State University and is a doctoral student at Pennsylvania State University. His research interests include magneto-optical spectroscopy and nanocluster carrier dynamics.

Hongjun Zheng earned his M.S. in Physical Chemistry from University of Science and Technology of China and is currently a doctoral student at Pennsylvania State University. His research interests include ultrafast spectroscopy and nanocluster carrier dynamics.

Kenneth L. Knappenberger, Jr., is a Professor of Chemistry at The Pennsylvania State University where he leads a research effort focused on development and use of laser spectroscopy methods for understanding nanoscale structure-dependent carrier dynamics. He was a postdoctoral researcher at University of California, Berkeley (2005−2008) and earned his Ph.D. at The Pennsylvania State University in 2005. He started his independent career at Florida State University (2008−2017) and became Head of the Magneto-optics Program at the National High Magnetic Field Laboratory, Tallahassee, in 2016.

REFERENCES

(1) Parker, J. F.; Fields-Zinna, C. A.; Murray, R. W. The Story of a Monodisperse Gold Nanoparticle: $Au_{25}L_{18}$. *Acc. Chem. Res.* **2010**, *43*, 1289−1296.

(2) Yi, C.; Zheng, H.; Tvedte, L.; Ackerson, C. J.; Knappenberger, K. L. Nanometals: Identifying the Onset of Metallic Behavior. *J. Phys. Chem. C* **2015**, *119*, 6307−6314.

(3) Haynes, C.; Van Duyne, R. Plasmon-Sampled Surface-Enhanced Raman Excitation Spectroscopy. *J. Phys. Chem. B* **2003**, *107*, 7426−7433.

(4) Halas, N. J.; Lal, S.; Chang, W. S.; Link, S.; Nordlander, P. Plasmons in Strongly Coupled Metallic Nanostructures. *Chem. Rev.* **2011**, *111*, 3913−3961.

(5) Valden, M.; Lai, X.; Goodman, D. W. Onset of Catalytic Activity of Gold Clusters on Titania with the Appearance of Nonmetallic Properties. *Science* **1998**, *281*, 1647−1650.

(6) Jin, R. Quantum Sized, Thiolate-protected Nanocrystals. *Nanoscale* **2010**, *2*, 343−362.

(7) Jarrett, J. W.; Zhao, T.; Johnson, J. S.; Knappenberger, K. L. Investigating Plasmonic Structure-Dependent Light Amplification and Electronic Dynamics Using Advances in Nonlinear Optical Microscopy. *J. Phys. Chem. C* **2015**, *119*, 15779−15800.

(8) Zhao, T.; Jarrett, J. W.; Johnson, J. S.; Park, K.; Vaia, R. A.; Knappenberger, K. L. Plasmon Dephasing in Gold Nanorods Studied Using Single-Nanoparticle Interferometric Nonlinear Optical Microscopy. *J. Phys. Chem. C* **2016**, *120*, 4071−4079.

(9) Zhu, M.; Aikens, C. M.; Hollander, F. J.; Schatz, G. C.; Jin, R. Correlating the Crystal Structure of a Thiol-Protected Au_{25} Cluster and Optical Properties. *J. Am. Chem. Soc.* **2008**, *130*, 5883−5885.

(10) Stoll, T.; Sgrò, E.; Jarrett, J. W.; Réhault, J.; Oriana, A.; Sala, L.; Branchi, F.; Cerullo, G.; Knappenberger, K. L. Superatom State-Resolved Dynamics of the $Au_{25}(SC_8H_9)_{18}^-$ Cluster from Two-Dimensional Electronic Spectroscopy. *J. Am. Chem. Soc.* **2016**, *138*, 1788−1791.

(11) Green, T. D.; Herbert, P. J.; Yi, C.; Zeng, C.; McGill, S.; Jin, R.; Knappenberger, K. L. Characterization of Emissive States for Structurally Precise $Au_{25}(SC_8H_9)_{18}^0$ Monolayer-Protected Gold Nanoclusters Using Magnetophotoluminescence Spectroscopy. *J. Phys. Chem. C* **2016**, *120*, 17784−17790.

(12) Herbert, P. J.; Mitra, U.; Knappenberger, K. L. Variable-Temperature Variable-Field Magnetic Circular Photoluminescence (VTVH-MCPL) Spectroscopy for Electronic-Structure Determination in Nanoscale Chemical Systems. *Opt. Lett.* **2017**, *42*, 4833−4836.

(13) Hartland, G. V. Optical Studies of Dynamics in Noble Metal Nanostructures. *Chem. Rev.* **2011**, *111*, 3858−3887.

(14) Sonnichsen, C.; Franzl, T.; Wilk, T.; von Plessen, G.; Feldmann, J.; Wilson, O.; Mulvaney, P. Drastic Reduction of Plasmon Damping in Gold Nanorods. *Phys. Rev. Lett.* **2002**, *88*, 077402.

(15) Coenen, T.; Schoen, D. T.; Mann, S. A.; Rodriguez, S. R. K.; Brenny, B. J. M.; Polman, A.; Brongersma, M. L. Nanoscale Spatial Coherent Control over the Modal Excitation of a Coupled Plasmonic Resonator System. *Nano Lett.* **2015**, *15*, 7666−7670.

(16) Stagg, S. M.; Knappenberger, K. L., Jr.; Dowgiallo, A. M.; Chandra, M. Three-Dimensional Interfacial Structure Determination of Hollow Gold Nanopshere Aggregates. *J. Phys. Chem. Lett.* **2011**, *2*, 2946−2950.

(17) Green, T. D.; Yi, C.; Zeng, C.; Jin, R.; McGill, S.; Knappenberger, K. L. Temperature-Dependent Photoluminescence of Structurally-Precise Quantum-Confined $Au_{25}(SC_8H_9)_{18}^0$ and $Au_{38}(SC_{12}H_{25})_{24}$ Metal Nanoparticles. *J. Phys. Chem. A* **2014**, *118*, 10611−10621.

(18) Wu, Z.; Jin, R. On the Ligand's Role in the Fluorescence of Gold Nanoclusters. *Nano Lett.* **2010**, *10*, 2568−2573.

(19) Weerawardene, K. L. D. M.; Aikens, C. M. Theoretical Insights into the Origin of Photoluminescence of Au25(SR)18- Nanoparticles. *J. Am. Chem. Soc.* **2016**, *138*, 11202−11210.

(20) Walter, M.; Akola, J.; Lopez-Acevedo, O.; Jadzinsky, P. D.; Calero, G.; Ackerson, C. J.; Whetten, R. L.; Grönbeck, H.; Häkkinen, H. A. Unified View of Ligand-Protected Gold Clusters as Superatom Complexes. *Proc. Natl. Acad. Sci. U. S. A.* **2008**, *105*, 9157−9162.

(21) Aikens, C. M. Geometric and Electronic Structure of $Au_{25}(SPhX)_{18}^-$ (X = H, F, Cl, Br, CH_3, and OCH_3). *J. Phys. Chem. Lett.* **2010**, *1*, 2594−2599.

(22) Green, T. D.; Knappenberger, K. L. Relaxation Dynamics of $Au_{25}L_{18}$ Nanoclusters Studied by Femtosecond Time-Resolved Near Infrared Transient Absorption Spectroscopy. *Nanoscale* **2012**, *4*, 4111−4118.

(23) Yi, C.; Zheng, H.; Herbert, P. J.; Chen, Y.; Jin, R.; Knappenberger, K. L. Ligand- and Solvent-Dependent Electronic Relaxation Dynamics of $Au_{25}(SR)_{18}^-$ Monolayer-Protected Clusters. *J. Phys. Chem. C* **2017**, *121*, 24894−24902.

(24) Yi, C.; Tofanelli, M.; Ackerson, C.; Knappenberger, K. L. Optical Properties and Electronic Energy Relaxation of Metallic $Au_{144}(SR)_{60}$ Nanoclusters. *J. Am. Chem. Soc.* **2013**, *135*, 18222−18228.

(25) Zheng, H.; Tofanelli, M.; Ackerson, C.; Knappenberger, K. L. Composition-dependent electronic energy relaxation dynamics of metal domains as revealed by bimetallic $Au_{144-x}Ag_x(SC_8H_9)_{60}$ monolayer-protected clusters. *Phys. Chem. Chem. Phys.* **2017**, *19*, 14471−14477.

DOI: 10.1021/acs.accounts.8b00096
Acc. Chem. Res. 2018, 51, 1433−1442